Supporting Information

Overcoming the Reactivity-Stability Challenge in Catalytic Water Treatment through Spatial Confinement

Zhonghao Wan[1], Seung Hee Chae[1], Aidan Francis Meese[1], Obinna Nwokonkwo[1,2], Leslie Arrazolo[1], Kwan Lam Yip[1], Xiaohan Ma[1], Shengdong Liu[3], Christopher Muhich[2], Dengjun Wang[4], Haoran Wei[3], Jae-Hong Kim[1,*]

[1] Department of Chemical and Environmental Engineering, Yale University, New Haven, CT, USA
[2] Chemical Engineering Program, School for Engineering of Matter, Transport, & Energy, Arizona State University, Tempe, AZ, USA
[3] Department of Civil and Environmental Engineering, University of Wisconsin–Madison, Madison, WI, USA
[4] Department of Agricultural and Biological Engineering, University of Florida, Gainesville, FL, USA

Corresponding author's address: jaehong.kim@yale.edu

Table of Contents

(arranged in chronological order corresponding to the main text)

(Nanotechnology Enabled Water Treatment Center, $[H_2O_2]$ = 10 mM, [THI] = [CLO] = [IMI] = 1 μM, pH = 6.2±0.1, $[CO_3^{2-}]$ = 10 mg L^{-1}, $[HCO_3^-]$ = 10 mg L^{-1}, $[Cl^-]$ = 2 mg L^{-1}, $[SO_4^{2-}]$ = 5 mg L^{-1}, $[Na^+]$ = 40 mg L^{-1}, [NOM] = 5 mg L^{-1}, reaction time = 1 h, standard deviations (n = 3) were presented).

Supplementary Figure 41. Water permeability of FeOF/GO membrane with NOM fouling.

Supplementary Figure 42. SEM and SEM-mapping images of rod-like FeOF.

Supplementary Figure 43. Graphene oxide membrane embedded with rod-like FeOF.

Supplementary Figure 44. GO and FeOF suspensions displaying Tyndall effect under laser emission.

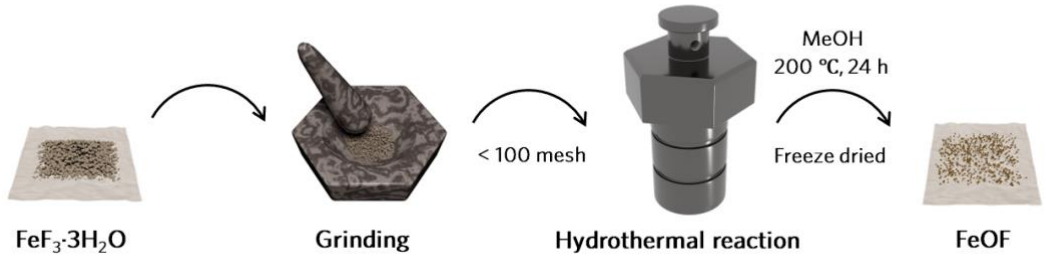

Supplementary Figure 1. Schematic diagram for two-dimensional FeOF synthesis.

Note: 33.4 mg $FeF_3 \cdot 3H_2O$ was added into 16 mL methanol in a 20 mL Teflon reactor. The mixture would be sonicated for 5 min before the vessel was sealed and transferred into 200 °C mechanical convection oven (ThermoFisher Scientific, USA). The reaction lasted 24 h and then allowed to cool down under ambient conditions. The as-prepared orangish powder was washed with pure ethanol and milli-Q water for three times, respectively. Then, it would be frozen in the lab fridge at -20 °C and freeze-dried in a 2.5 L benchtop freeze dryer (Labconco, USA) at -84 °C overnight.

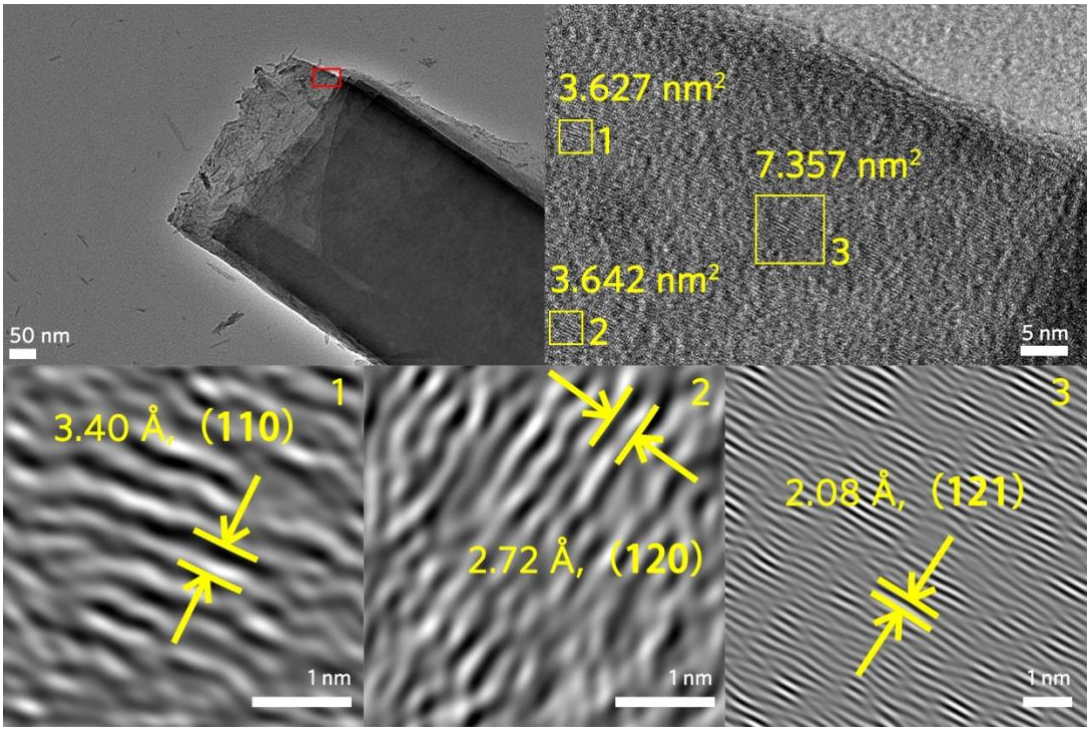

Supplementary Figure 2. TEM images of the FeOCl.

Note: All lattice spacings of FeOCl were referred to PDF Card No. 01-079-5319. The images were inverse FFT treated using Digital Micrograph software.

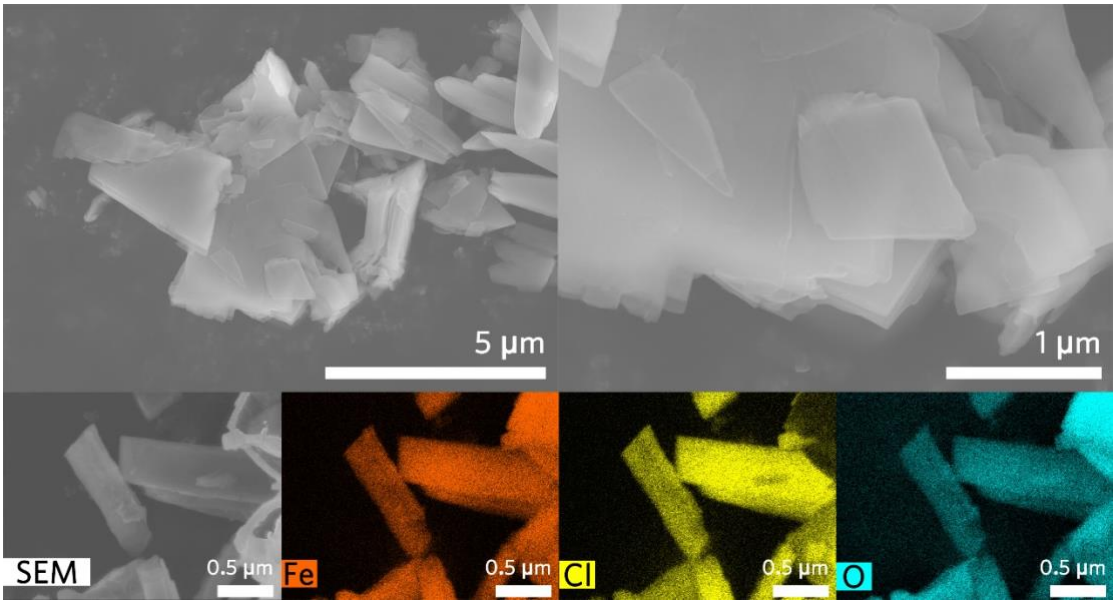

Supplementary Figure 3. SEM and SEM-EDS mapping images of the FeOCl.

Note: If not otherwise specified, the time duration was fixed at 5 min during SEM mapping.

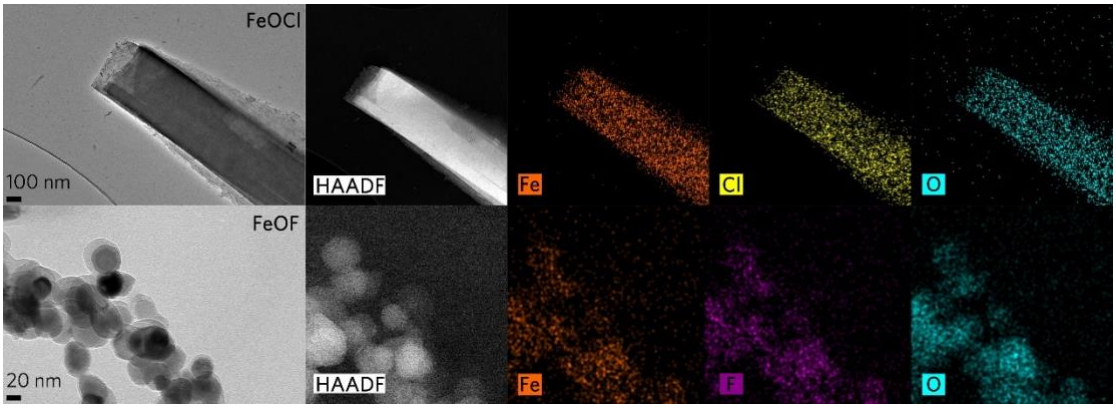

Supplementary Figure 4. TEM and TEM-EDS mapping images of the FeOCl and FeOF.

Note: If not otherwise specified, the time duration was fixed at 10 min during TEM mapping.

Supplementary Table 1. Elemental compositions determined by total digestion.

	Fe	O	Cl or F	Estimated structure [1]
FeOCl	34.5±0.8%	30.1±2.5%	35.4±1.7%	$Fe_{1.14}OCl_{1.17}$
FeOF	28.3±1.5%	16.1±3.3%	55.6±1.8%	$Fe_{1.75}OF_{3.45}$
Acid washed [2] FeOCl	31.1±1.6%	30.3±2.4%	38.6±0.8%	$Fe_{1.02}OCl_{1.27}$
Acid washed [2] FeOF	25.8±2.1%	17.5±2.8%	56.7±0.7%	$Fe_{1.47}OF_{3.24}$
Spent FeOCl [3]	32.1±0.6%	67.9±0.6%	0 [5]	$Fe_{0.47}OCl_{0}$
Spent FeOF [3]	28.1±1.1%	33.0±3.7%	38.9±2.6%	$Fe_{0.85}OF_{1.18}$
Spent FeOF/GO [4]	26.5±0.5%	19.7±2.6%	53.8±2.1%	$Fe_{1.34}OF_{2.69}$
Exfoliated FeOF [6]	53.9±0.8%	33.6±6.0%	12.5±5.2%	$Fe_{1.60}OF_{0.37}$

[1] 50 mg materials or pieces of spent membranes were digested using microwave digestor in 10 mL acid in $HCl:HNO_3$ = 3:1.
[2] Fresh materials were treated with 1 mM HCl, stirred at room temperature for 10 min, centrifuged, washed with DI water until neutral pH, then dried in a vacuum oven at 60 °C overnight.
[3] After 12 h reaction.
[4] After 14 d reaction in simulated contaminated water.
[5] Below the detection limit of IC.
[6] Fresh FeOF was exfoliated under probe sonication for 5 min with 70% amplitude.

Note: The elements were normalized based on O. According to the results, the overall leaching of Fe for both oxyhalides were not severe compared to the leaching of halides.

Supplementary Text 1. Total digestion of iron oxyhalides and membranes.

50 mg vacuum-dried FeOCl or FeOF or 5 pieces of spent membranes was put into the Teflon-lined microwave reaction vessels containing 10 mL acid in a ratio of $HCl:HNO_3$ = 3:1. The vessels were sealed and placed into microwave digestor (ETHOS easy high performance microwave digestion system, USA) for undergoing 2 h of microwave digestion at 220 ℃ with a ramping rate of 10 ℃ min^{-1}. After cooling down overnight, the liquid in reaction vessels was volumed to 10 mL using 5% HNO_3 and measured by ICP-OES and IC for different ions.

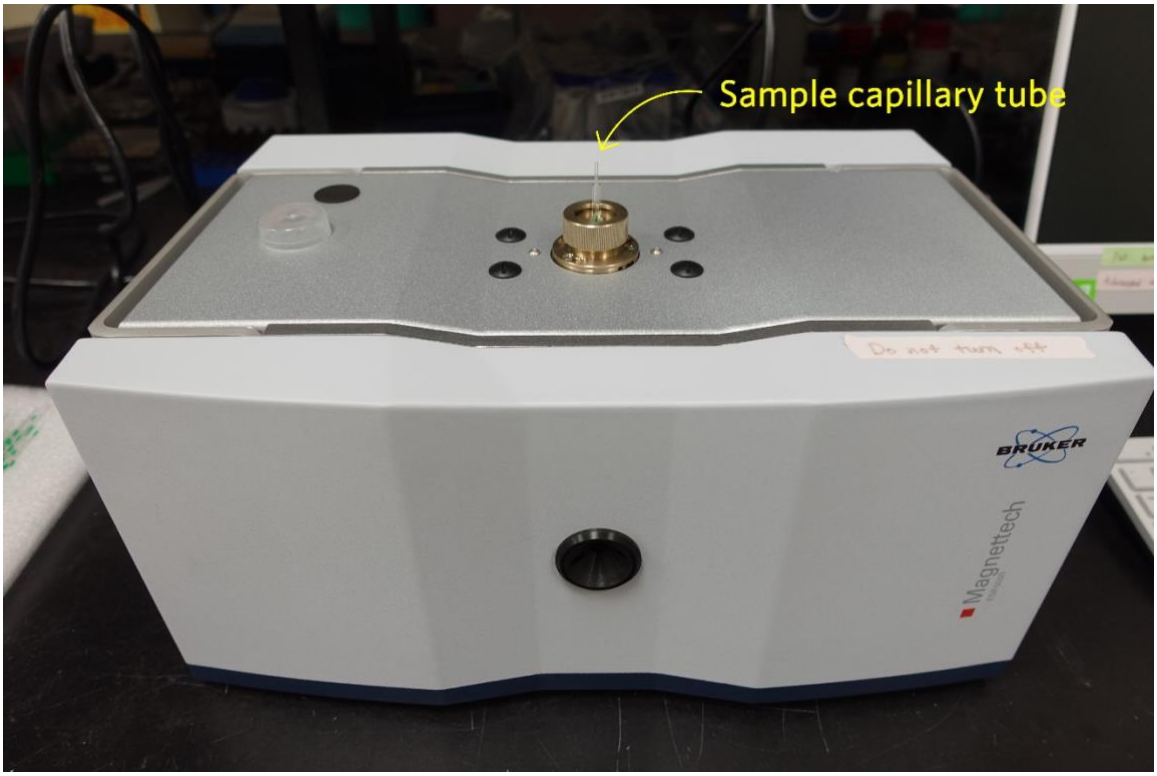

Supplementary Figure 5. EPR platform for in situ monitoring radical generation.

Supplementary Text 2. Detailed procedure for EPR tests.

Electron paramagnetic resonance (EPR) spectra were obtained using the ESR5000 spectrometer (Bruker, Germany) under the following conditions: resonance frequency of 9.82 GHz, microwave power of 20.07 mW, modulation frequency of 100 kHz, modulation amplitude of 1.0 G, sweep width of 100 G, time constant of 40.96 ms, sweep time of 83.93 s, and receiver gain of 2.0×10^4 at room temperature. 100 or 200 mM solution of 5,5-dimethyl-1-pyrroline-N-oxide (DMPO) was used as the spin-trapping agent in non-buffered solution. Peak intensities of the DMPO–OH signals at specific time intervals were used to assess H_2O_2 activation efficiency.

EPR tests on *powder-form* materials were performed to assess their intrinsic capability to generate radicals. These experiments were conducted in small vials containing an aqueous DMPO solution. After adding H_2O_2 to initiate the reaction, the system was allowed to react for 1 minute. Subsequently, a portion of the reacted bulk solution was withdrawn using 50 μL capillary tubes (Drummond Scientific Company, USA), sealed with capillary sealing compound (Fisher Scientific, USA), and immediately analyzed using the EPR instrument for radical quantification.

In contrast, the EPR measurements involving *membrane-form* materials were conducted under continuous-flow conditions. In this setup, DMPO and H_2O_2 were premixed prior to passing through the membrane. The reaction was initiated during the flow-through process by contacting with the catalysts, and samples were periodically collected using capillary tubes from the outlet of the reaction vessel (**Fig. 4a**). These reacted solutions were immediately sealed and analyzed by EPR to quantify radical species.

The time interval between sampling and measurement was strictly maintained at less than 1 minute.

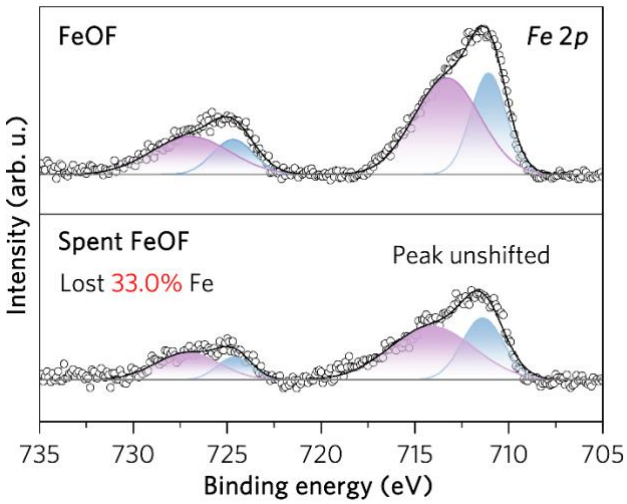

Supplementary Figure 6. *Fe 2p* XPS spectrum of the FeOF before and after H_2O_2 activation.

Note: The loss of element proportion was calculated based on the XPS signal intensity. All XPS tests were conducted under the same configurations in one day. The equipment was X-ray photoelectron spectroscopy (XPS) with a Versa Probe II scanning XPS microprobe (Physical Electronics, USA) using monochromatic Al Kα radiation (1486.6 eV), which was located at West Campus Materials Characterization Core of Yale University. Noting that the XPS mainly investigates the elements within ~10 nm depth of the material surface, not overall.

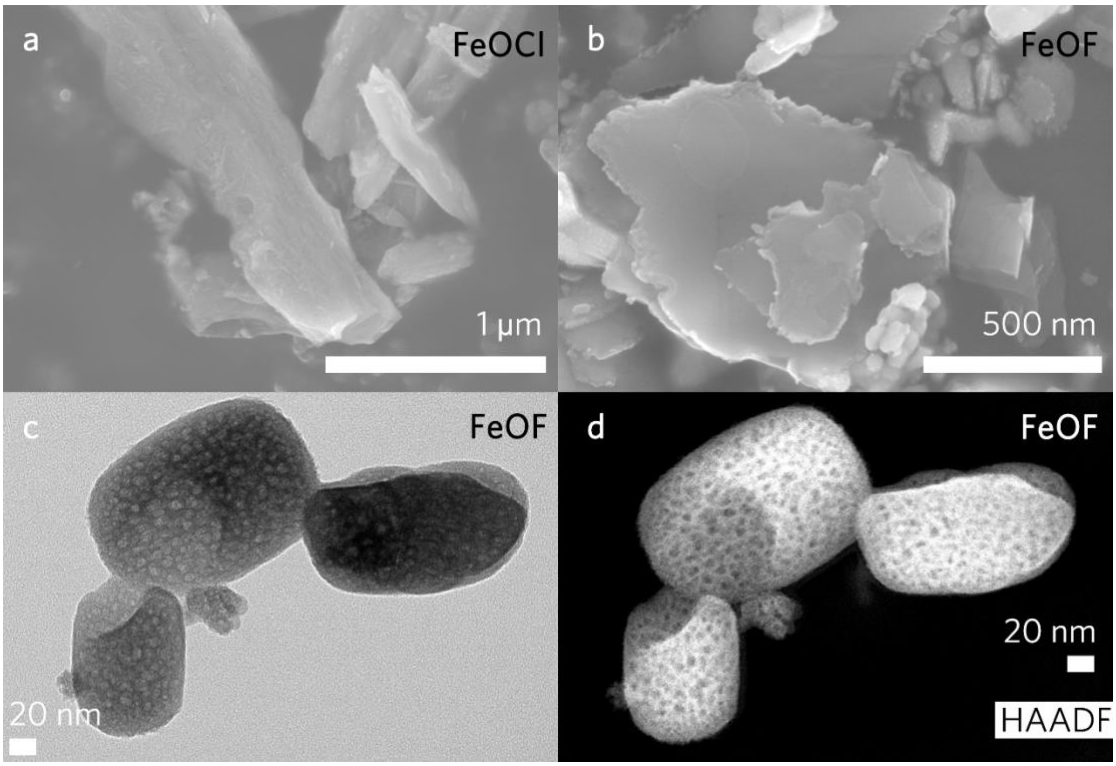

Supplementary Figure 7. **a-b**, SEM images of the FeOCl and FeOF after H_2O_2 activation; **c-d**, TEM and HAADF-TEM images of the FeOF after H_2O_2 activation.

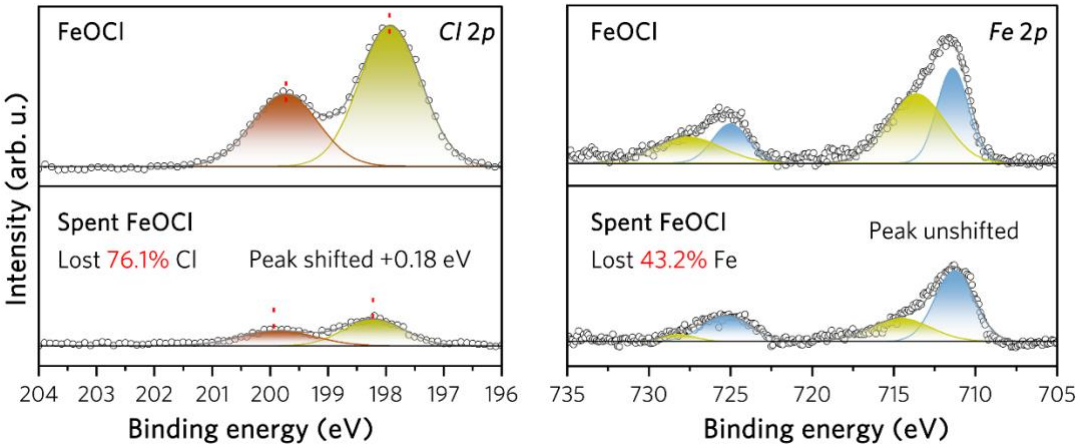

Supplementary Figure 8. *Cl 2p* and *Fe 2p* XPS spectra of the FeOCl before and after H_2O_2 activation.

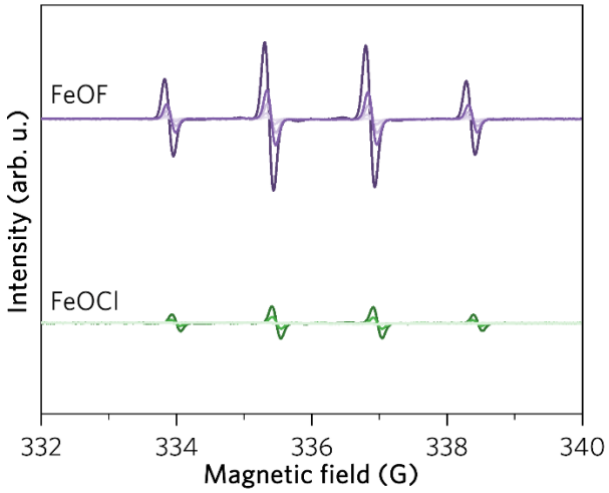

Supplementary Figure 9. EPR signals of the reacted FeOCl and FeOF activating H_2O_2 with different pre-reaction time ([catalyst] = 1 g L^{-1}, [H_2O_2] = 10 mM, contact time = 1, 2, 3 or 4 h, a lighter color indicative of a longer contact time, [DMPO] = 200 mM, reaction time = 1 min, pH = 6.2±0.1).

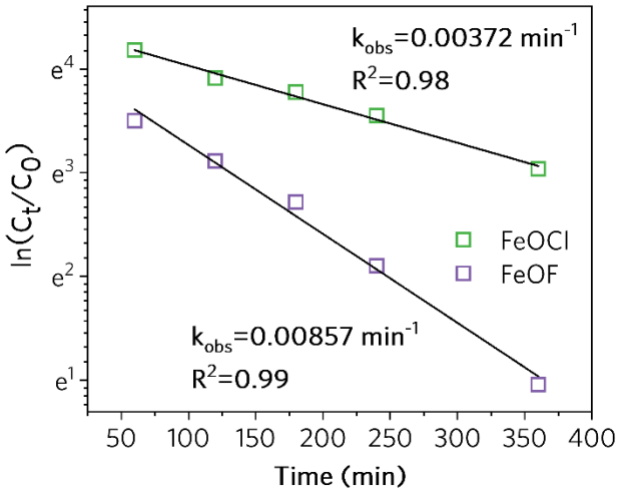

Supplementary Figure 10. H_2O_2 consumption rates over time in suspension systems ([catalyst] = 1 g L^{-1}, [H_2O_2] = 10 mM, pH = 6.2±0.1).

Supplementary Text 3. H_2O_2 measurement.

Hydrogen peroxide (H_2O_2) was quantified using 4-carboxyphenylboronic acid (CPBA). First, 1 mL stock solution of CPBA was prepared at a concentration of 50 μM. For each measurement, 10 μL of the sample was taken on a regular time interval into the CPBA stock solution. After incubating the mixture at room temperature for 30 min to allowing the reaction to complete, the absorbance of each sample was measured at 300 nm using a UV-Vis spectrophotometer.

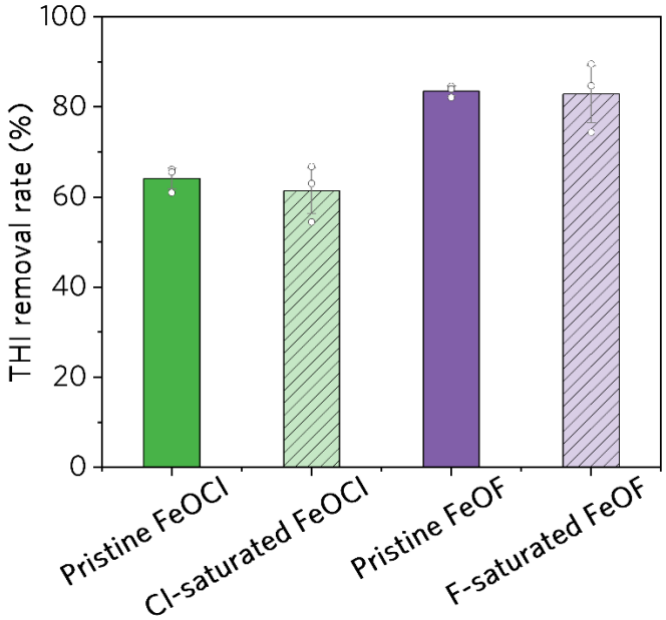

Supplementary Figure 11. Comparison of catalytic performance between pristine iron oxyhalides and halide-saturated iron oxyhalides ([catalyst] = 1 g L^{-1}, [H_2O_2] = 10 mM, pH = 6.2±0.1, reaction time = 60 min, standard deviations (n = 3) were presented).

Note: The iron oxyhalides were pre-saturated under 0.5 M halide environment overnight. Then, the halide-saturated materials were collected by vacuum filtration over

a PES membrane (0.45 μm) without washing. After drying in the vacuum oven at 60 °C, the halide-saturated materials were used for catalytic testing directly.

Supplementary Table 2. Textural characteristics of membranes.

	FeOF	PES substrate	GO	FeOF/GO	FeOF topping	CNT	FeOF/CNT
Surface area, S_{BET} (m^2 g^{-1}) [1]	3.19	2.89	7.10	6.41	7.94	981.17	850.35
Micropore area, S_{micro} (m^2 g^{-1}) [2]	0.078	0.93	0.48	1.63	0.58	592.85	499.99
External surface area, S_{ext} (m^2 g^{-1})	3.11	1.95	6.61	4.78	7.36	388.31	350.36
Total pore volume, V_{total} (cm^3 g^{-1})	0.0031	0.0024	0.0069	0.0069	0.0075	0.54	0.51
Micropore volume, V_{micro} (cm^3 g^{-1})	0	0.00035	0.00015	0.00064	0.00024	0.23	0.20

[1] Brunauer–Emmett–Teller (BET) method
[2] Barrett–Joyner–Halenda (BJH) method.

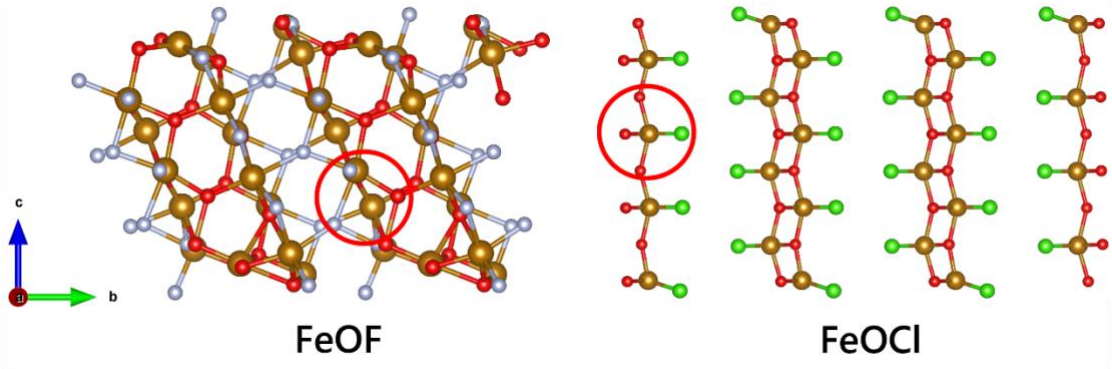

Supplementary Figure 12. Relaxed structures of iron oxyhalides (bond information of the circled units is shown in **Figure 2c**).

Supplementary Table 3. EXAFS fitting parameters at the Fe K–edge for samples.

Sample	Path	CN [1]	R(Å) [2]	σ^2($\times 10^{-3}$ Å^2) [3]	E_0(ev) [4]	R-factor
Fe foil	Fe-Fe1	8	2.46+/-0.02	4.76+/-1.78	-2.41+/-2.65	0.008
	Fe-Fe2	6	2.85+/-0.01	5.29+/-2.95		
Fe_2O_3	Fe-O	6	2.26+/-0.09	2.77+/-0.53	4.38+/-1.65	0.005
	Fe-Fe	4	3.33+/-0.12	2.12+/-0.38		
Fe_3O_4	Fe-O	4	1.94+/-0.02	10.03+/-4.68	-3.73+/-2.54	0.03
	Fe-O	12	3.18+/-0.03	10.03+/-4.3		
	Fe-Fe	12	3.46+/-0.04	8.80+/-5.66		
FeO	Fe-O	6	2.34+/-0.05	2.62+/-4.24	-2.59+/-2.32	0.009
	Fe-Fe	12	3.02+/-0.02	13.2+/-4.54		
FeOCl	Fe-O/Cl	3.16+/-0.35	1.97+/-0.01	10.59+/-1.91	-2.00+/-1.47	-0.0068
FeOF	Fe-O/F	5.71+/-0.23	1.97+/-0.005	6.96+/-0.62	-0.76+/-0.59	0.0009
FeOF/GO	Fe-O/F	5.28+/-0.47	2.02+/-0.02	3.03+/-1.16	2.46+/-1.07	0.004
Spent FeOF/GO	Fe-O/F	5.35+/-0.66	2.03+/-0.03	3.66+/-0.82	1.77+/-1.06	0.007
FeOF/CNT	Fe-O/F	5.15+/-0.58	2.04+/-0.03	3.60+/-2.58	2.05+/-1.29	0.010
Spent FeOF/CNT	Fe-O	4.19+/-0.45	1.98+/-0.02	7.54+/-2.66	0.54+/-1.15	0.018

[1] CN, coordination number.
[2] R, distance between absorber and backscatter atoms.
[3] σ^2, Debye-Waller factor to account for both thermal and structural disorders.
[4] ΔE_0, inner potential correction; *R* factor indicates the goodness of the fit. S_0^2 was fixed to 0.71, according to the experimental EXAFS fit of Fe foil by fixing CN as the known crystallographic value. A reasonable range of EXAFS fitting parameters: $0.600 < S_0^2 < 1.000$; $CN > 0$; $\sigma^2 > 0$ Å^2; $|\Delta E_0| < 15$ eV; *R* factor < 0.02.

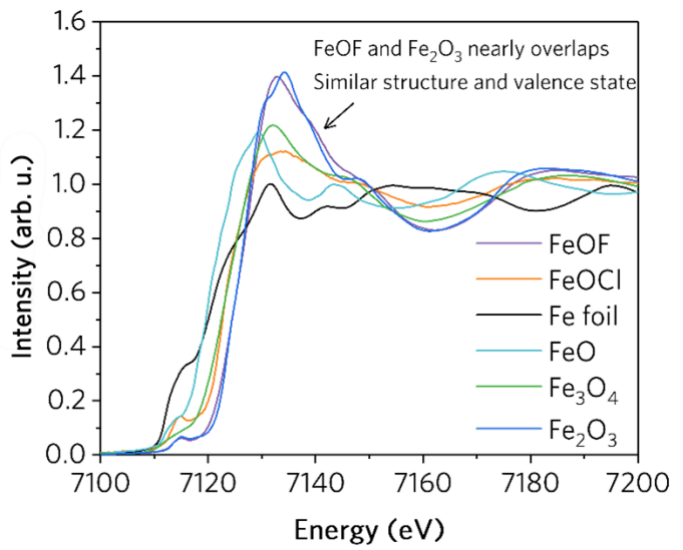

Supplementary Figure 13. XANES spectra of iron oxyhalides and reference materials.

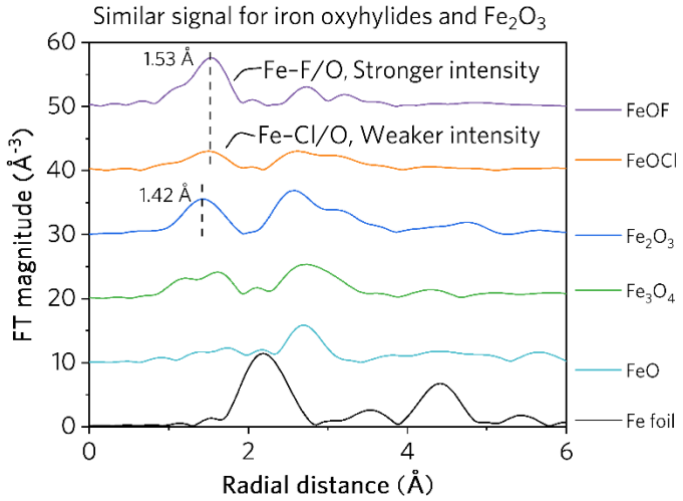

Supplementary Figure 14. EXAFS spectra of iron oxyhalides and reference materials.

Note: Peak positions indicate the similarity of Fe cores in iron oxyhalides and Fe_2O_3.

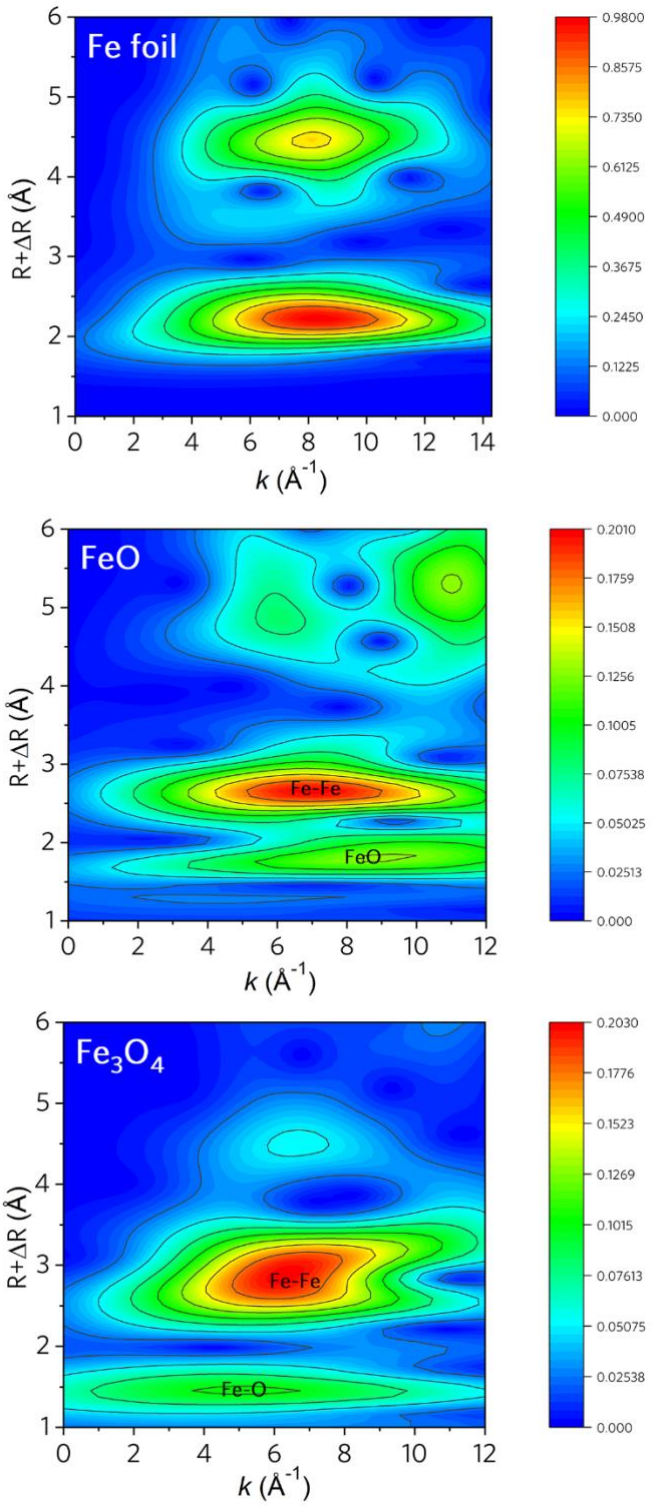

Supplementary Figure 15. Fourier transform of k^2-weighted EXAFS spectra of reference materials.

Supplementary Text 4. Bader charge analysis.

The FeOF structure is more compact than FeOCl, which has intra-lattice channels with exposed Cl atoms. In FeOF, bulk Fe atoms exhibit octahedral coordination (Fig. 2c), but on the surface, only 25% retain octahedral coordination with exposed F atoms, while the remaining 75% are undercoordinated (25% with a coordination number of five and 50% with a coordination number of four) with no singly bound F atoms exposed. Thus, the FeOF surface presents a greater diversity of metal sites compared to the bulk. The Fe-F bond lengths vary with coordination where octahedral surface sites have the shortest bond (1.78 Å), followed by the undercoordinated surface sites (1.98 Å), with the bulk having the longest bonds (2.13 Å, on average), indicating stronger Fe-F bonds at the surface octahedral sites.

Similarly, FeOCl consists of bulk Fe atoms in octahedral coordination, but unlike FeOF, all surface Fe atoms are undercoordinated (coordination number five). The surface Fe-Cl bonds (2.42 Å) are slightly longer than bulk Fe-Cl bonds (2.38 Å), suggesting that surface Cl atoms are less tightly bound. Hence, while both FeOF and FeOCl have bulk octahedral Fe cores coordinated with halide and oxygen atoms, the longer Fe-X bonds in FeOCl relative to FeOF indicate that Cl atoms are more loosely held and, thus, more susceptible to displacement under chemical action.

Bader charge analysis reveals that surface F atoms in FeOF have a lower charge (0.66 e^-) at octahedral Fe sites compared to those at undercoordinated sites (0.71 e^-), consistent with the latter being bonded to more Fe atoms. The bulk F atom charges match those of surface F atoms at undercoordinated sites. In contrast, FeOCl surface Cl atoms all have equal charge (0.54 e^-), close to the bulk average (0.51 e^-). The higher charge on the surface F atoms in FeOF compared to Cl atoms in FeOCl aligns with the greater electronegativity of F. Additionally, the higher electron density on F atoms implies stronger electronic Fe-F interactions relative to Fe-Cl, consistent with shorter Fe-F bonds. Consequently, Cl atoms in FeOCl are more easily displaced than F atoms in FeOF as observed in our experiments.

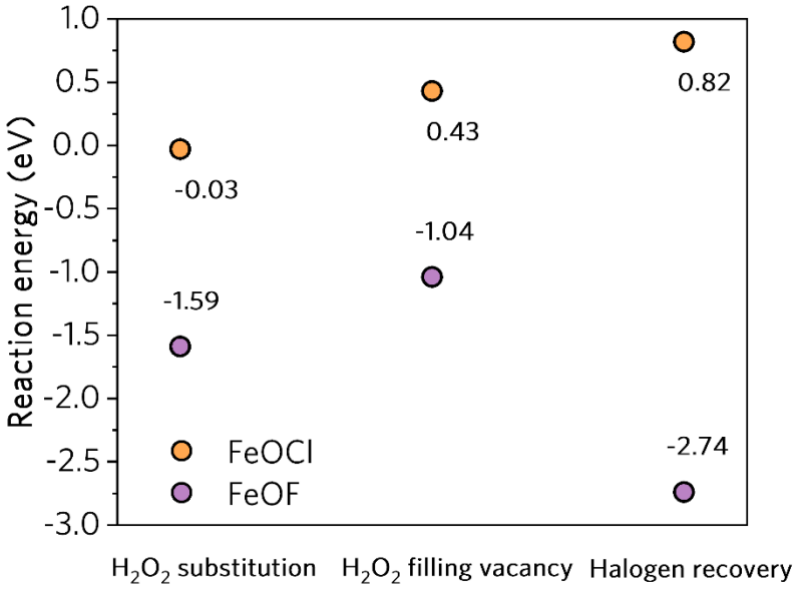

Supplementary Figure 16. Simulations of reaction energies on H_2O_2 reacting with FeOCl or FeOF.

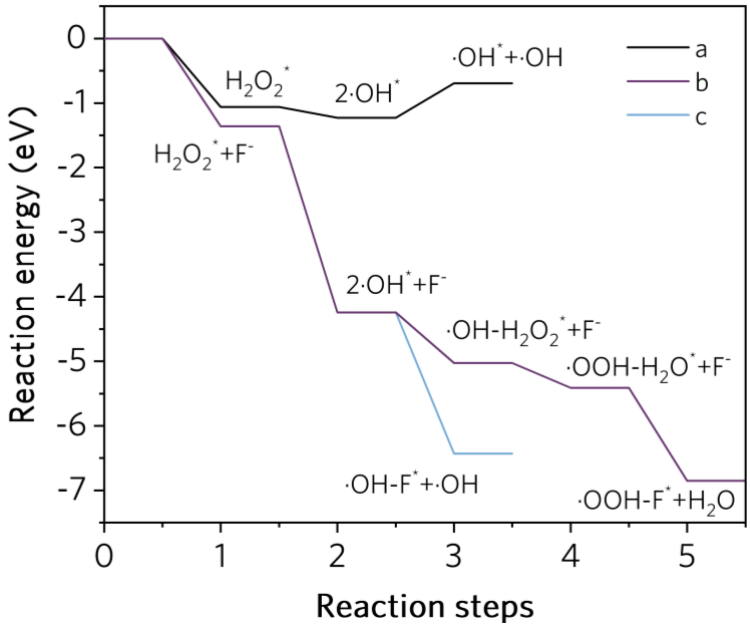

Supplementary Figure 17. Simulations of reaction energies of the pathways in which FeOF activates H_2O_2: (a) direct conversion of H_2O_2 to •OH on FeOF without fluorine release, (b) conversion of H_2O_2 to •OH on FeOF involving F^- regeneration and formation of an intermediate •OOH species, and (c) conversion of H_2O_2 to •OH on FeOF involving F^- regeneration without the formation of a •OOH intermediate.

Supplementary Text 5. Synthesis of single layer graphene oxide.

Single layer graphene oxide was exfoliated from pristine graphene oxide paste. First, 1 g of graphene oxide paste was dissolved in 25 mL of Milli-Q water and stirred for 24 hours. The resulting suspension was then probe sonicated under 70% amplitude for 30 minutes in an ice-bath. After sonication, the mixture was centrifuged at 6000 rpm for 10 minutes to remove large, unexfoliated particles. The supernatant was decanted, yielding a 6 mg mL^{-1} single-layer graphene oxide suspension.

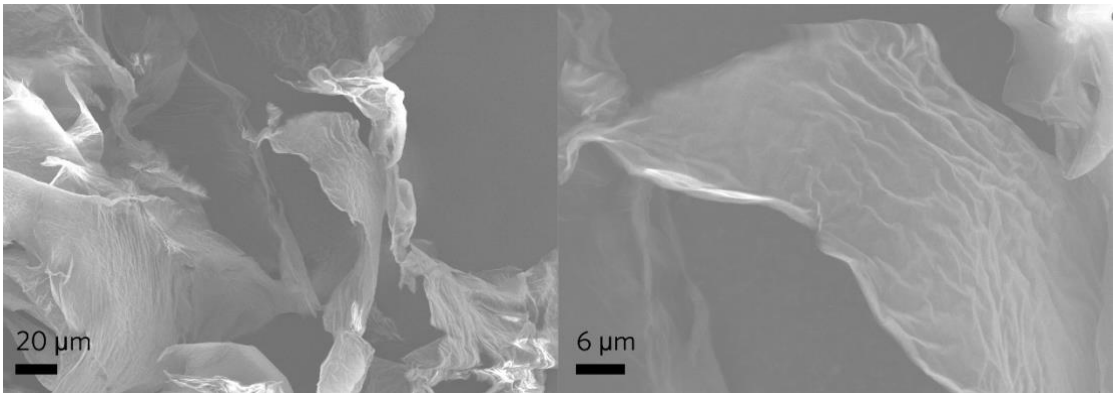

Supplementary Figure 18. SEM images of the exfoliated graphene oxide.

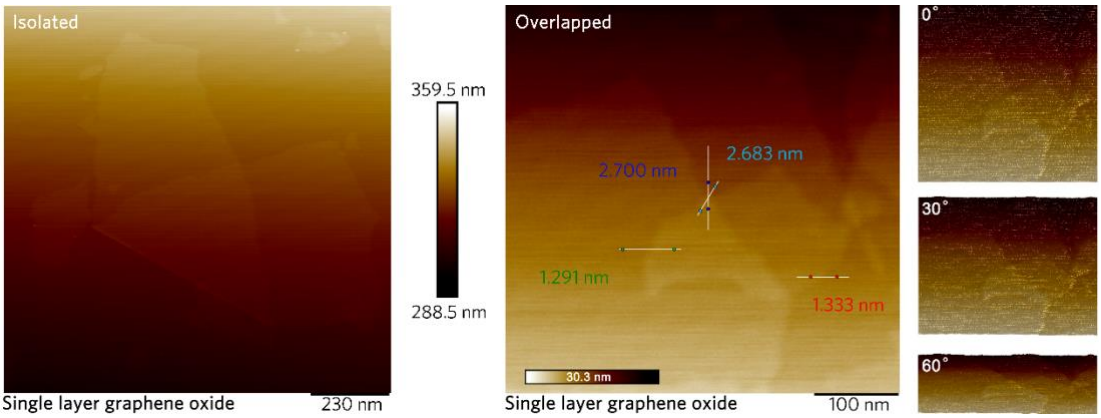

Supplementary Figure 19. Direct observation of the isolated single layer graphene oxide and the stacked single layer graphene oxide layers by 2D and 3D AFM images.

Note: All AFM images were taken on a mica layer, which was cleaned by 3M tape before each measurement. It should be noted that there is a spacing between the single layer graphene oxide and the mica substrate, which should be deducted when calculating the interlayer spacing between graphene oxide layers.

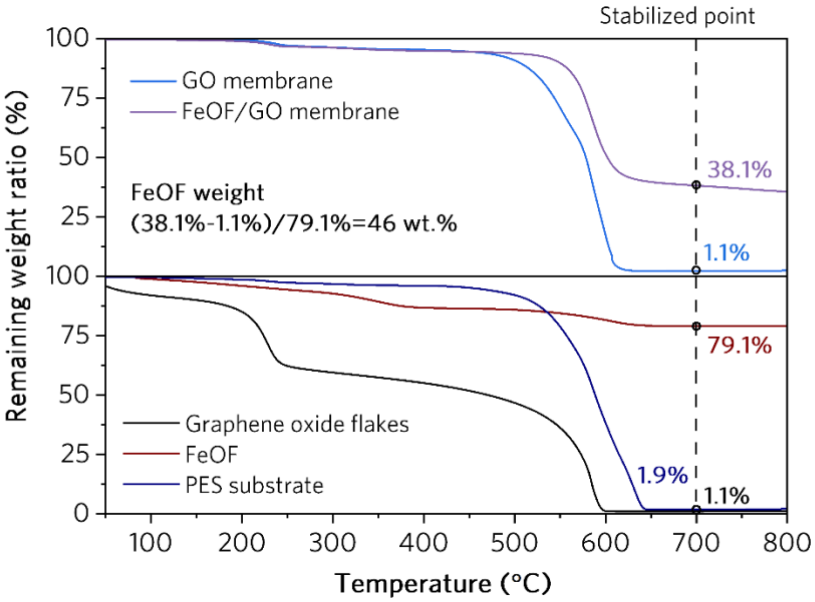

Supplementary Figure 20. TGA analysis of membranes and materials (Ar atmosphere, ramping at 10 °C min^{-1} from 50 to 800 °C).

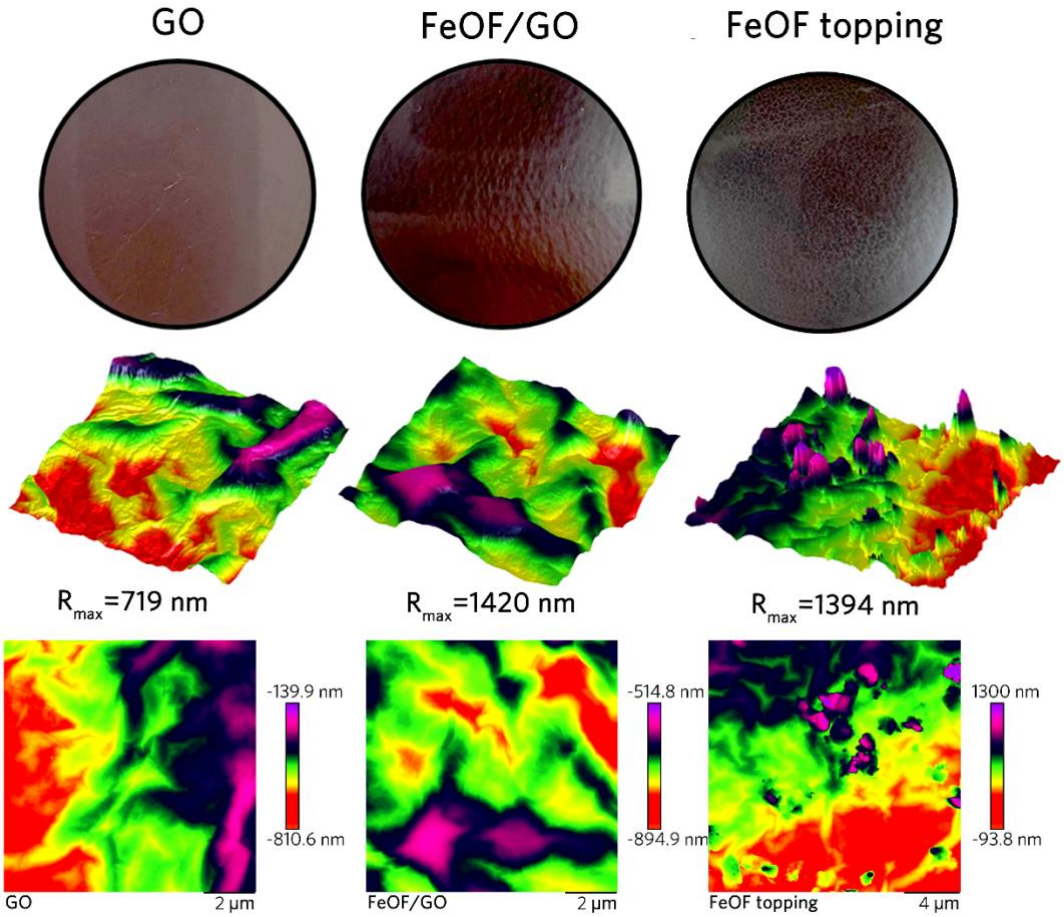

Supplementary Figure 21. Photos taken for membranes and roughness measured from AFM images of membranes.

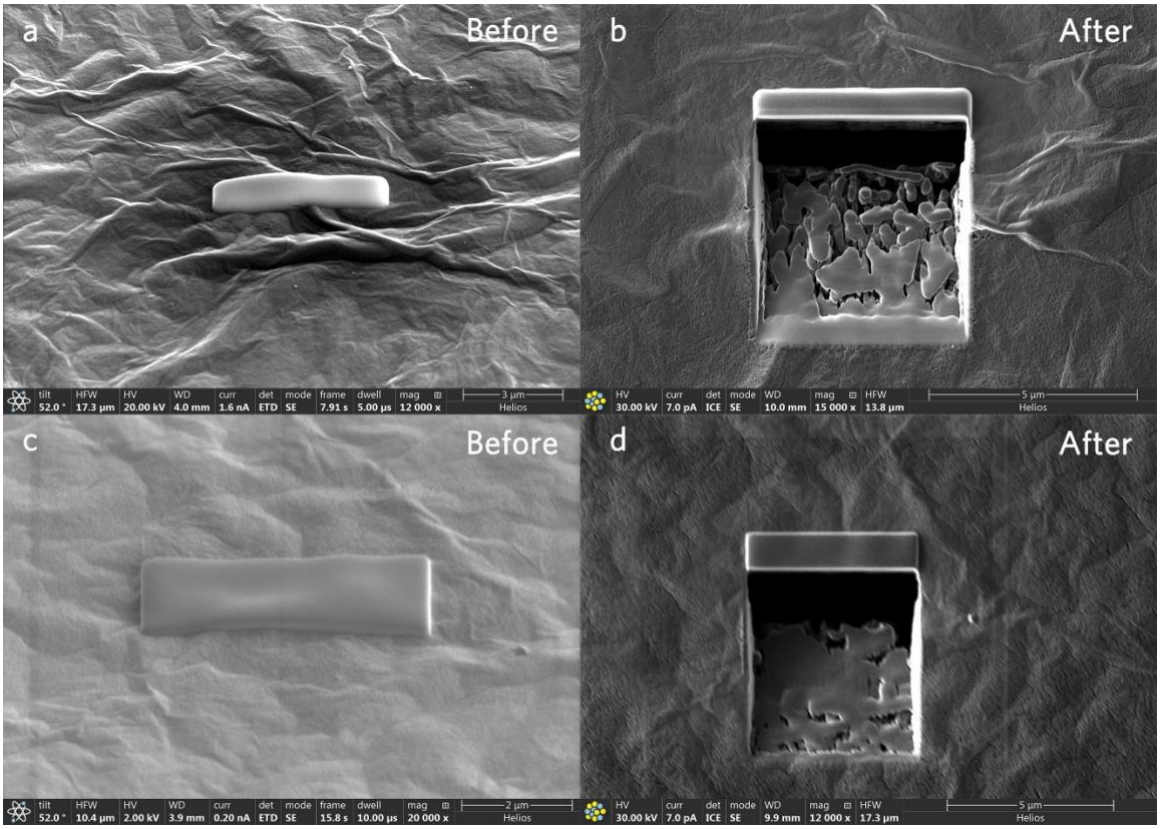

Supplementary Figure 22. **a**, GO membrane before emitting beam. **b**, top view of GO membrane after emitting beam. **c**, FeOF/GO membrane before emitting beam. **d**, top view of FeOF/GO membrane after emitting beam.

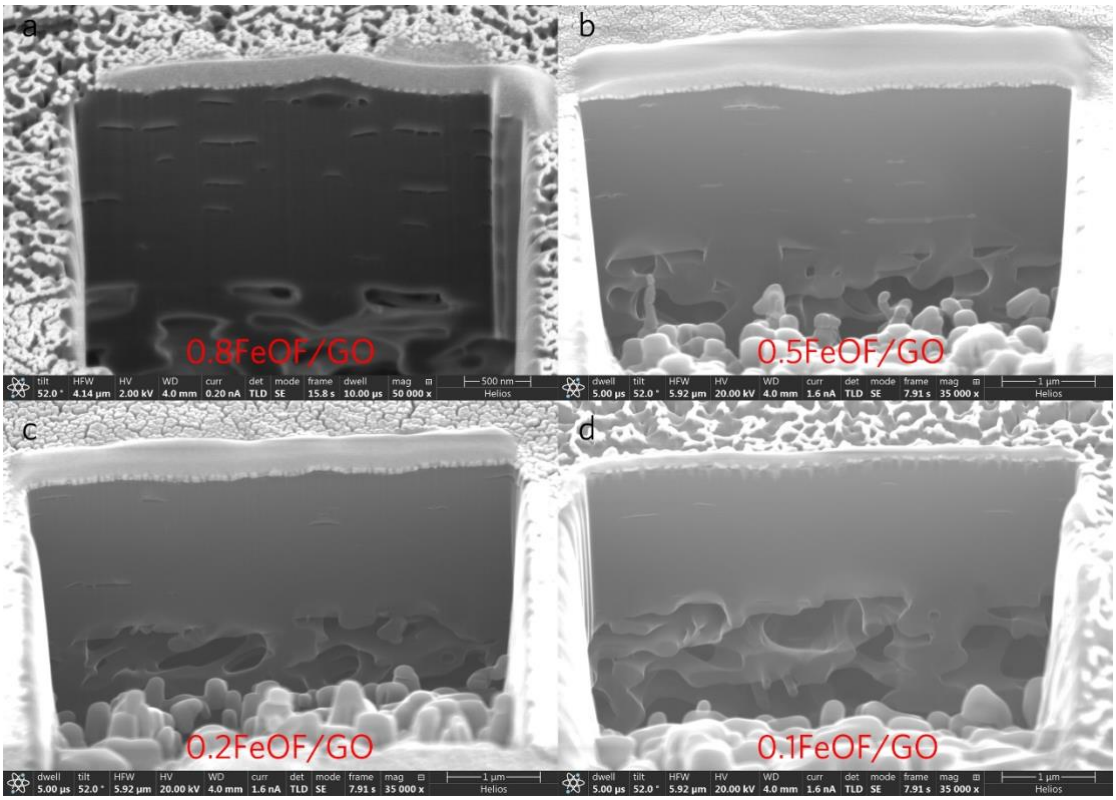

Supplementary Figure 23. FIB-SEM images of the different FeOF/GO membranes with varied FeOF addition (0.8, 0.5, 0.2 or 0.1 of the original amount).

Supplementary Text 6. Procedure for cross-sectional FIB-SEM analysis.

To prepare a cross-sectional view of a membrane using FIB-SEM on the ThermoFisher Helios G4 UX DualBeam, begin by mounting the membrane onto a sample holder with carbon tape or adhesive to ensure stability. Prior to testing, coat the membrane with a 50 nm layer of iridium (Ir) to enhance conductivity and reduce charging. Load the sample into the FIB-SEM chamber and pump it down to high vacuum. Tilt the sample to 52° to align the region of interest with the ion beam for optimal milling and observation. Calibrate the electron and ion beams, then set SEM imaging parameters. Deposit a 0.5 µm platinum (Pt) protective layer over the region of interest using the gas injection system to prevent damage during milling. Create a trench around the target area using the ion beam at 27 nA for initial milling, then polish the cross-section at 44 nA for a clearer surface. Capture high-resolution SEM images of the cross-section under optimized parameters.

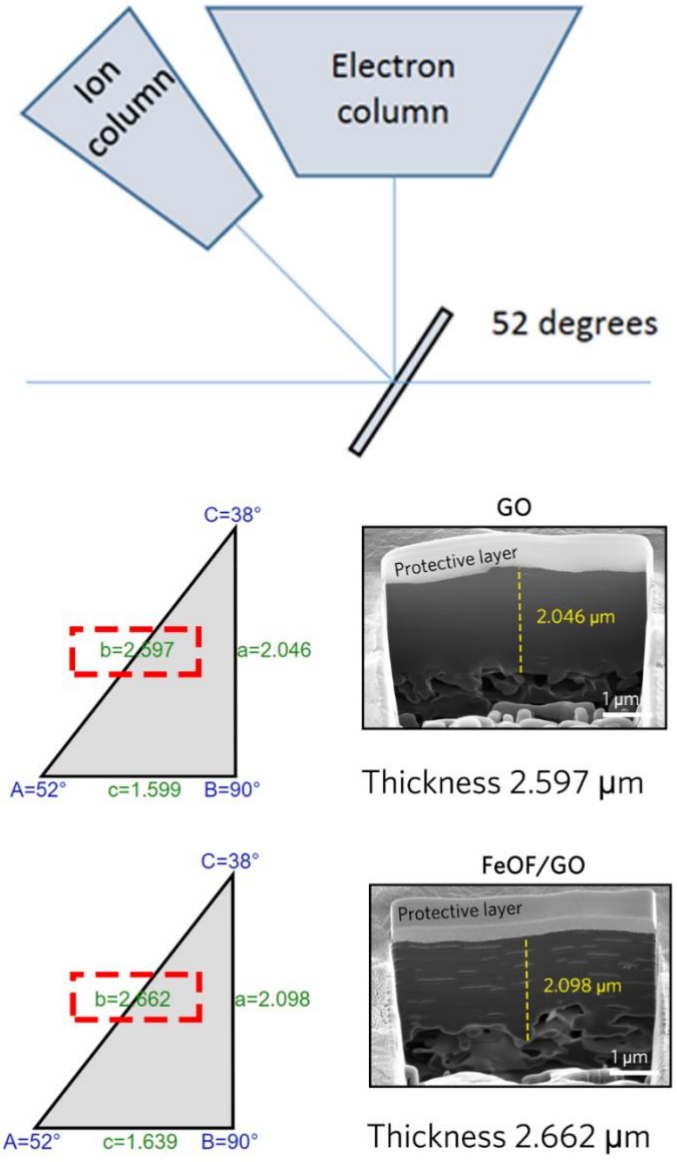

Supplementary Figure 24. Thickness of membranes calculated from FIB-SEM images. Note: The surface cut by ion beam was vertically flat, which promises it a valid method

to measure the membrane thickness. Common sample preparation protocol and technical features in microscopic techniques, such as liquid nitrogen cracking cooperating with SEM to calculate the membrane thickness, could not provide accurate results, because liquid nitrogen cracking is a physical process leading to uneven surface (although good for observing materials in interlayers as it is non-destructive with no heat involved) and the tilting angle between detector and sample holder in SEM will be of high uncertainty.

Supplementary Text 7. Preparing membrane samples for cross-sectional SEM analysis.

Membrane samples were vacuum-dried at 60°C overnight. The dried membranes were then immersed in liquid nitrogen (-196°C) for approximately 2 minutes using Dumont #3 tweezers. Once the membranes became brittle, pressure was carefully applied to both sides of the membranes until they broke. Membrane pieces with sharp and smooth fracture surfaces were selected for further cross-sectional analysis. It is important to note that this liquid nitrogen method helps preserve the original morphology of the alien materials (FeOF in this work) in membranes in the cross-sectional view.

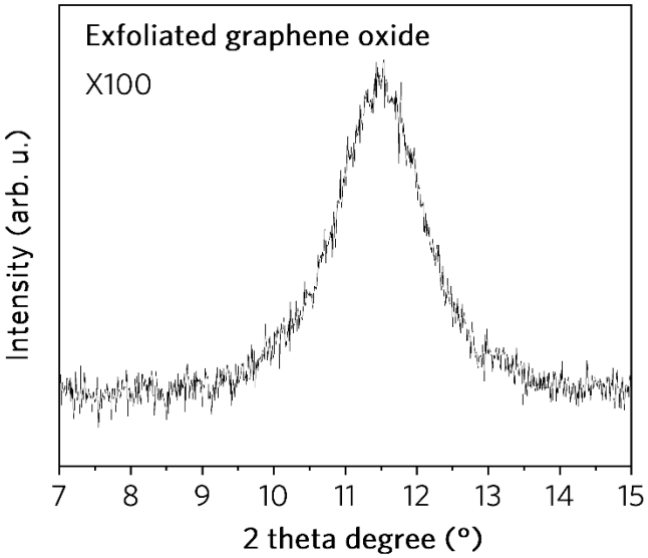

Supplementary Figure 25. XRD pattern of the exfoliated graphene oxide, zooming in by 100 times compared with the scale in **Figure. 3d**.

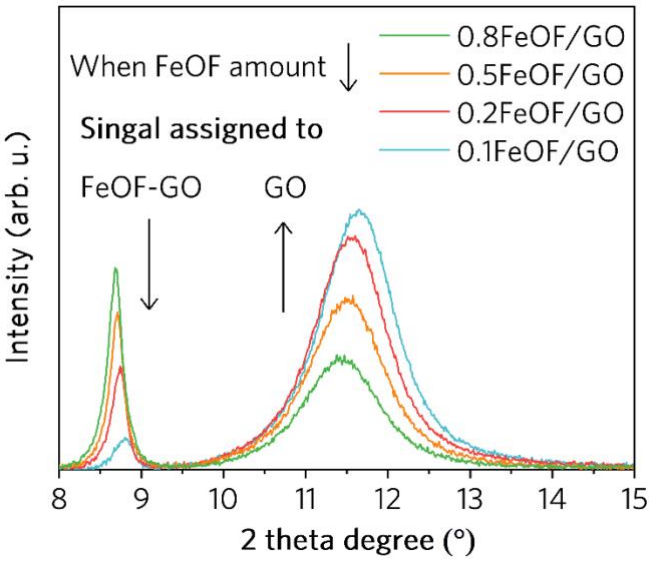

Supplementary Figure 26. XRD patterns of the different FeOF/GO membranes with varied FeOF addition (1.0, 0.8, 0.5, 0.2 or 0.1).

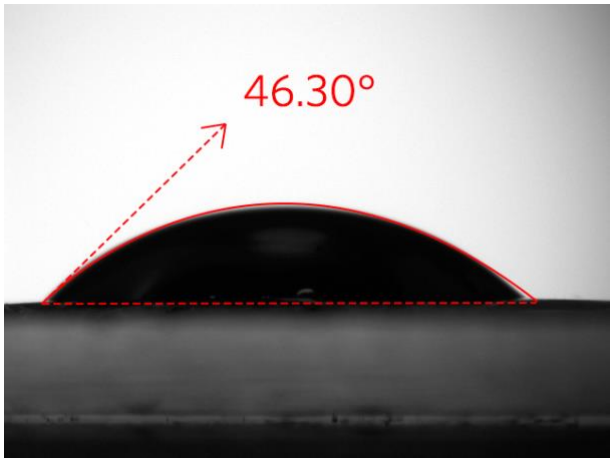

Supplementary Figure 27. Contact angle test of FeOF topping membrane.

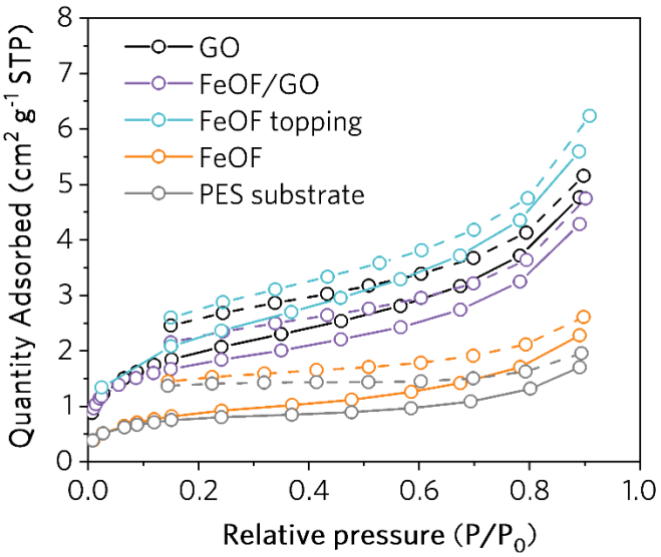

Supplementary Figure 28. N_2 adsorption-desorption isotherms of membranes and materials.

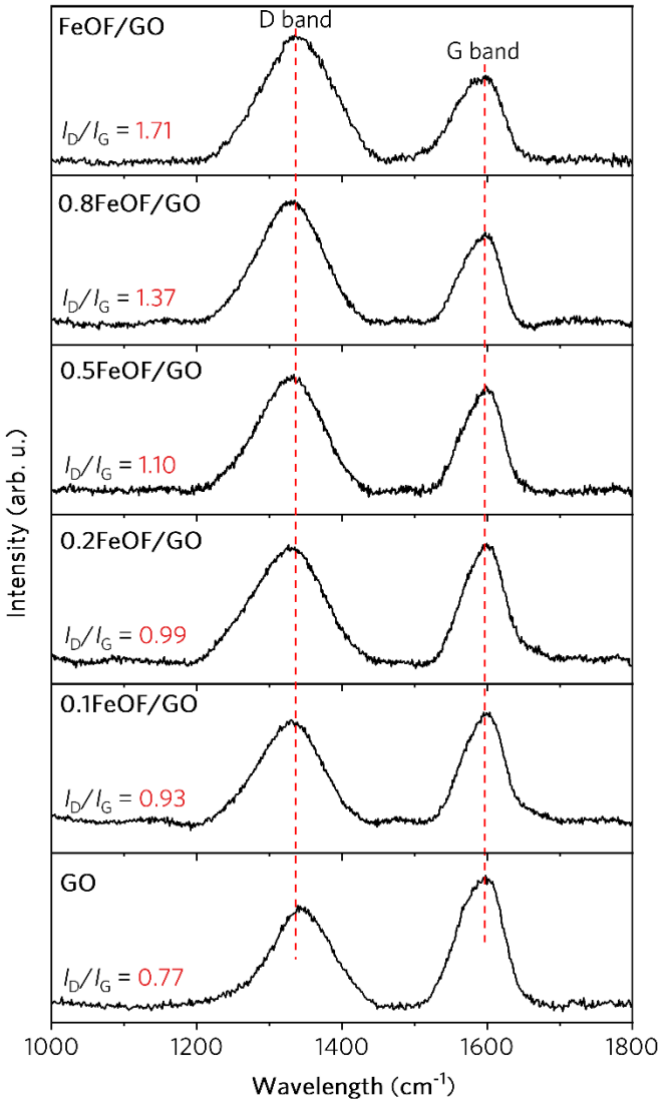

Supplementary Figure 29. Raman spectra of the different FeOF/GO membranes with varied FeOF addition (1.0, 0.8, 0.5, 0.2 or 0.1) and GO.

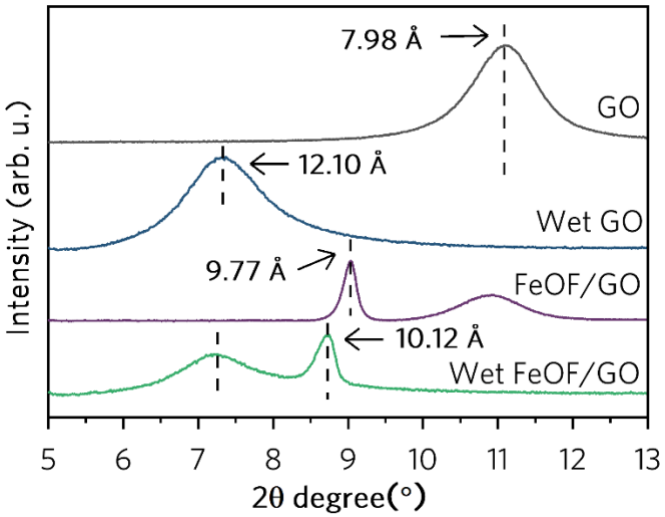

Supplementary Figure 30. XRD patterns of wet GO and FeOF/GO membranes.

Supplementary Text 8. Water saturation test to measure the inner volume of membranes.

The inner volume of the membranes was determined using a water saturation method, which translates the weight of water retained in the membrane pores. Specifically, the membranes were placed inside the flow-through membrane cell, and pressure was slowly increased until the moment effluent was observed at the outlet. The saturated membranes were then taken out, and any remaining surface water was gently wiped off using a Kimwipe. The weight change was divided by the density of water to calculate the inner volume. This procedure was repeated five times for accuracy.

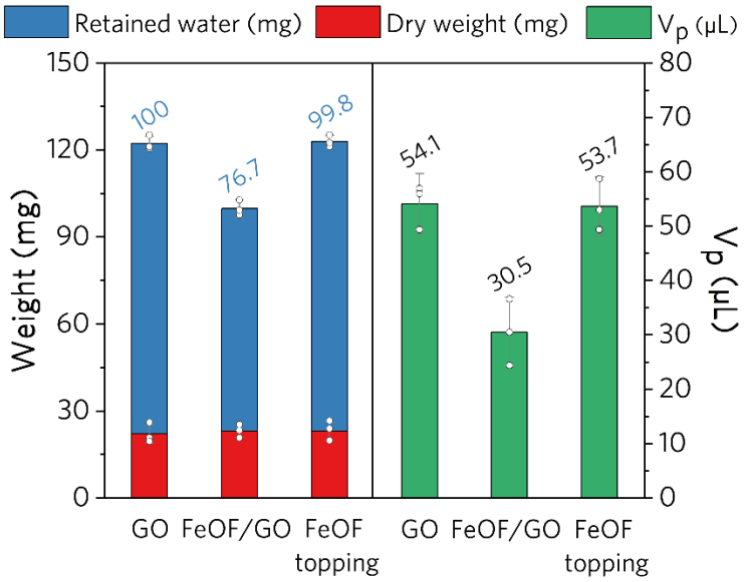

Supplementary Figure 31. Volume of water channels in the membranes where standard deviations (n = 3) were presented.

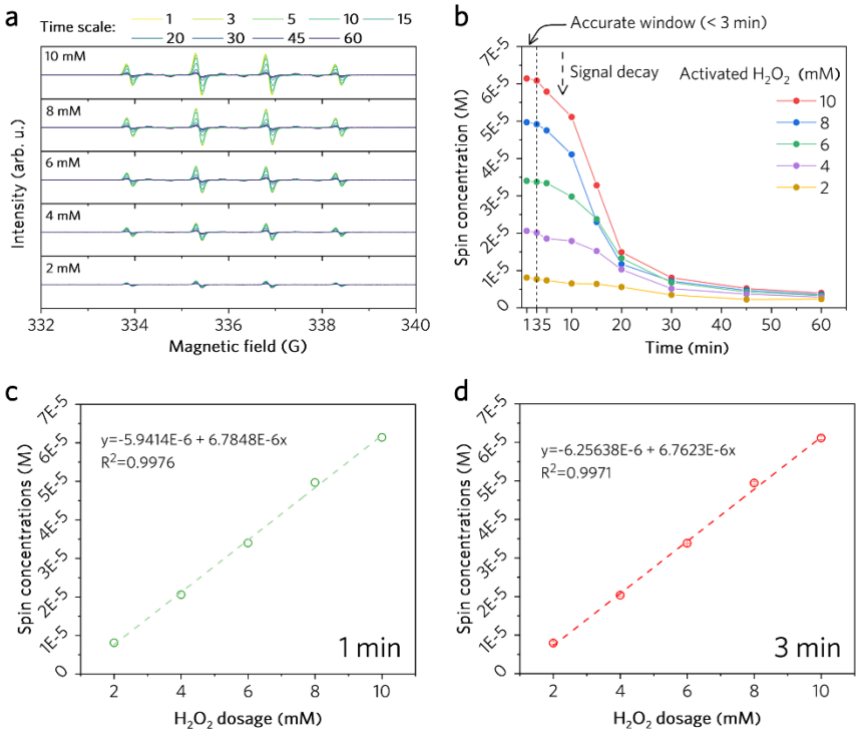

Supplementary Figure 32. **a**, Signals of DMPO–OH by fully activating different concentrations of H_2O_2 over time ([Fe^{2+}]:[H_2O_2] = 1:5, [H_2O_2] : [DMPO] = 1:20, pH = 3.0±0.1). **b**, accurate window when applying EPR to monitor DMPO–OH signal. **c**, standard curve for sampling within 1 min after reaction. **d**, standard curve for sampling within 3 min after reaction.

Note: Our results suggest that, if aiming for a valid quantification of the DMPO–OH signal in Fenton reactions, the time interval between sampling and measurement must be controlled to within 3 minutes. Based on the established standard signal intensity, H_2O_2 activation levels could be relatively quantified in the continuous-flow experiments using the DMPO as the probe chemical.

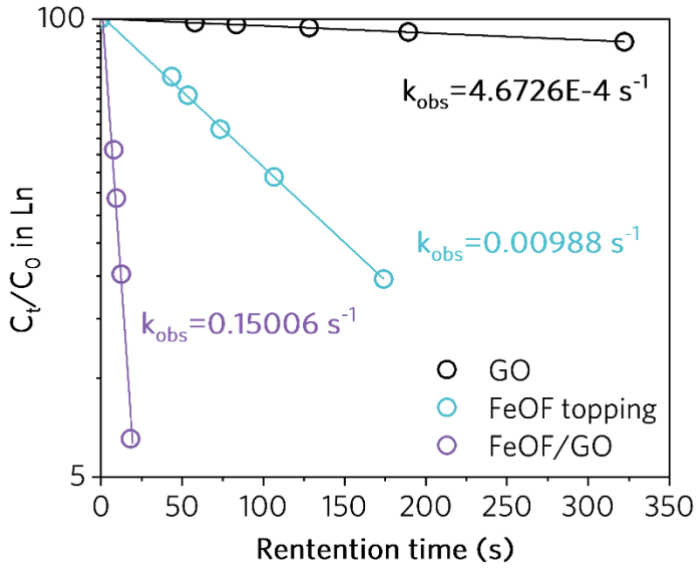

Supplementary Figure 33. Reaction kinetics of the membranes in the THI degradation ([H_2O_2] = 10 mM, [THI] = 10 μM, pH = 6.2±0.1, pressure = 2 bar).

Supplementary Table 4. Comparison of H_2O_2 activation performance in different systems.

System	pH	H_2O_2 to •OH conversion efficiency (%)	Probe chemical	Reference
Continuous flow				
FeOF/GO initially running	6.2±0.1	69.8%	DMPO	This work
FeOF/GO running for 1 h		64.5%		
FeOF/GO running 8 h		64.3%		
FeOF topping initially running		39.2%		
FeOF topping running for 1 h		8.57%		
FeOF topping running for 8 h		0		
GO membrane initially running		0		
Batch experiments				
FeOF	7	33.3%	Coumarin	[1]
FeOCl	7	0.0210%		
Ferrihydrite	3	0.0740%		
FeOCl	7	0.0733%	Terephthalic acid	[2]
ZrO_2–Fe_2O_3	7	0.236%		[3]
$BiFeO_3$	4.5	0.0122%		[4]
Fe_3O_4	4	52.5%	Benzoic acid	[5]
Cu_5/FeS_2	7	48.3%		[6]
FeS_2	7	5.34%		[6]
FeB	3	40.4%		[7]
DBC-FeO_x	3.5	25.1%		[8]
$CuFe_2O_4$	5	0.795%		[9]
Siderite	6	4.83%		[10]
nano-Fe_2O_3	5	0.540%		[11]
nano-Fe_3O_4	3	0.0871		[11]
meso-$CuFe_2O_4$	3	0.134%		[12]
CQDs-Fe(III)	5	5.05%		[13]
HS-$CuFe_2O_4$-σ	6.5	0.203%		[14]
CD-COOFe(III)	4.5	2.79%		[15]

Supplementary Table 5. Comparison of catalytic performance in different spatial confinement systems.

System	Pollutant	Oxidant	Removal Rate	Long-term performance	References
FeOF/GO membrane	Neonicotinoids	H_2O_2	~99% for 10 μM pollutants under continuous flow	>2-week continuous operation	This work
FeOOH/rGO hollow fiber membrane	Bisphenol A (BPA)	H_2O_2	95% in batch experiment, 5 min	No explicit long-term duration reported	[16]
$FeCo_2O_4$ embedded ceramic membrane	Sulfamethoxazole (SMX)	PMS	>99% in 3 min (batch); >95% in flow-through	Flow-through stability >180 min	[17]
Angstrom-confined Co-TiOx	BPA, Phenol, Rhodamine B	PMS	Up to ~100% (5–10 min)	Stable for 10+ cycles (batch mode); Flow-through stability not reported	[18]
Co_1-GO membrane	1,4-Dioxane	PMS	~90% in single-pass	>60 min stable performance under flow-through experiment	[19]

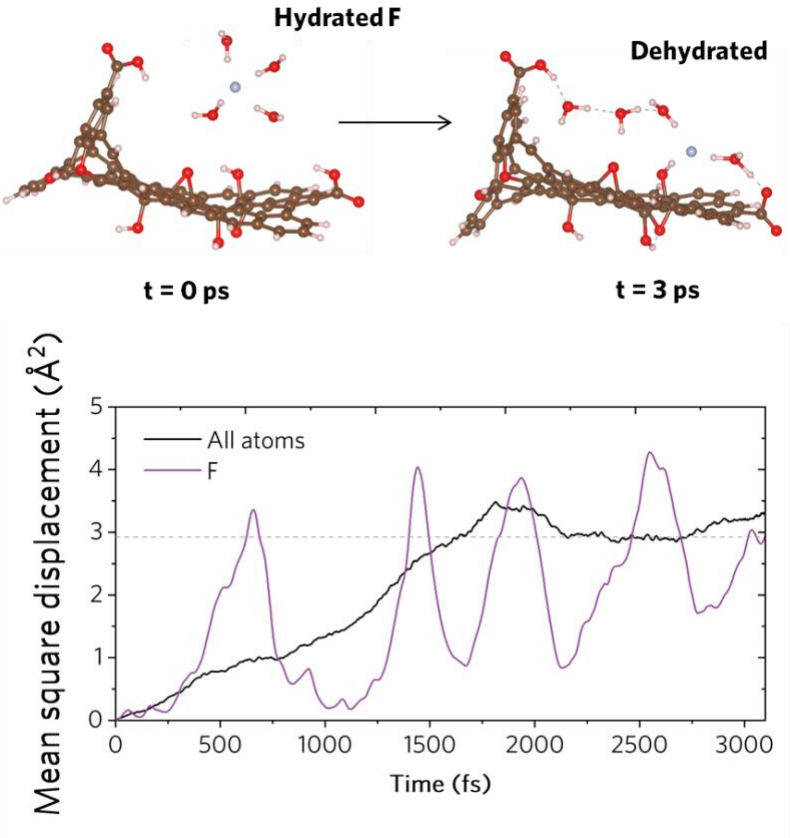

Supplementary Figure 34. Ab initio molecular dynamics (AIMD) simulations of hydrated fluoride confined by graphene oxide.

Supplementary Figure 35. SEM images of CNT and FeOF/CNT membranes and EDS mapping of FeOF in FeOF/CNT.

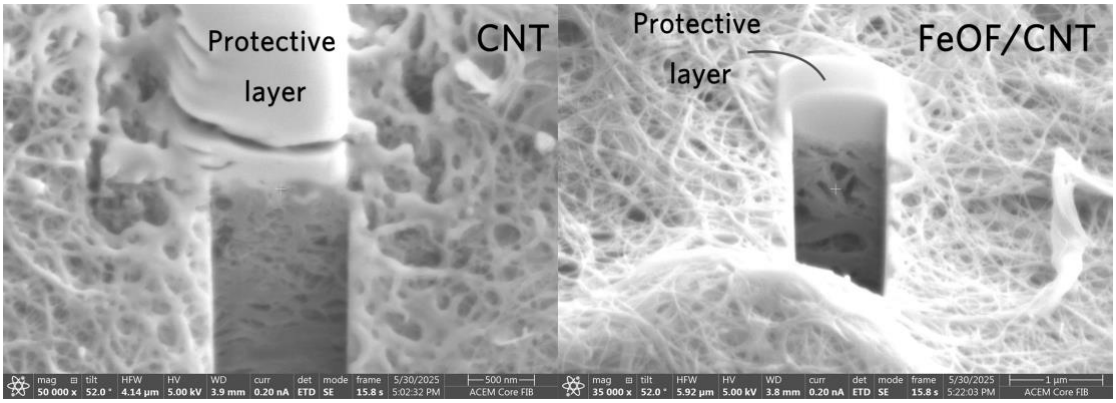

Supplementary Figure 36. FIB-SEM images of CNT and FeOF/CNT membranes.

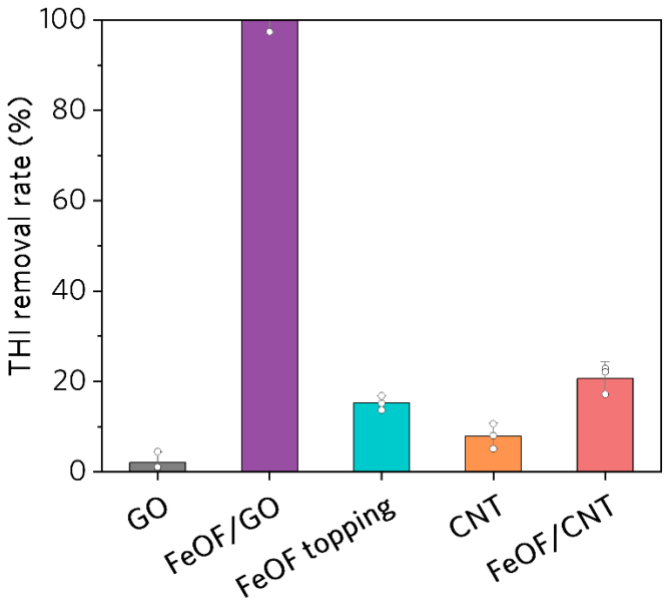

Supplementary Figure 37. THI removal at 2 h running time for different membrane systems where standard deviations (n = 3) were presented.

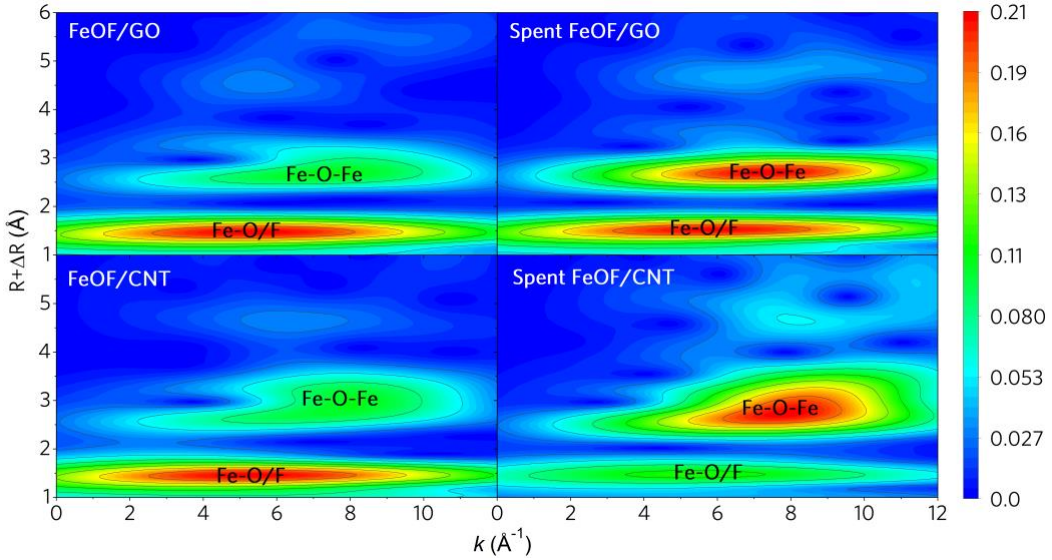

Supplementary Figure 38. Fourier transform of k^2-weighted EXAFS spectra of membranes.

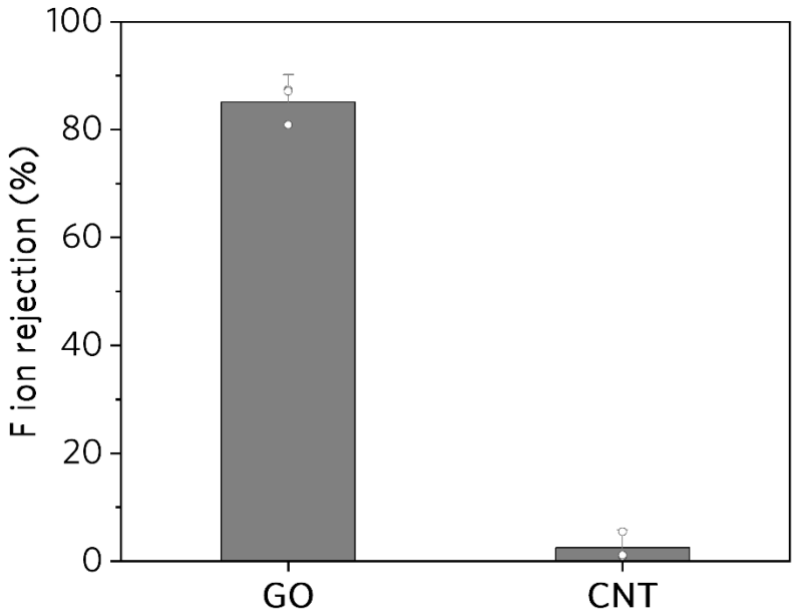

Supplementary Figure 39. F ion rejection by GO and CNT membranes with feeding F ion concentration of 100 mg L^{-1} where standard deviations (n = 3) were presented.

Supplementary Table 6. Compositions of contaminated well water adapted from the recipes of NEWT Center (Nanotechnology Enabled Water Treatment Center, USA).

Constituents	Parameters
Neonicotinoids	
THI	1 μM
CLO	1 μM
IMI	1 μM
NOM	5 mg L^{-1}
CO_3^{2-}	10 mg L^{-1}
HCO_3^-	10 mg L^{-1}
Cl^-	5 mg L^{-1}
SO_4^{2-}	5 mg L^{-1}
Na^+	40 mg L^{-1}
Ion strength	1.5 mM
pH	6.2±0.1
Temperature	22±1 ℃

Note: NEWT is a prestigious center Yale University collaborated with, and recipe was adapted from relevant literatures of the center.

Supplementary Text 9. Estimation of molecular diameter.

The molecular diameter of organic probes was calculated based on the van der Waals volume (V_{vdW}, $Å^3$/molecule), which was calculated according to **Equation S1**, taking into consideration the atomic and bond group contributions.

$$V_{vdW} = \sum \text{all atom contributions} - 5.92N_B - 14.7N_A - 3.8R_{NA} \quad \textbf{(S1)}$$

where N_B is the number of bonds, dimensionless; R_A is the number of aromatic rings, dimensionless; R_{NA} is the number of nonaromatic rings, dimensionless.

The number of bonds present (N_B) can be calculated by **Equation S2** as follows.

$$N_B = N - 1 + R_A + R_{NA} \quad \textbf{(S2)}$$

where N is the total number of atoms, dimensionless.

Accordingly, the volume of neonicotinoids can be calculated, i.e., thiamethoxam (THI, $C_8H_{10}ClN_5O_3S$), imidacloprid (IMI, $C_9H_{10}ClN_5O_2$), clothianidin ($C_6H_8ClN_5O_2S$, CLO). Taking THI as an example,

$$V_{vdW} = (8 \times V_C) + (10 \times V_H) + (3 \times V_O) + (1 \times V_{Cl}) + (5 \times V_N) + (1 \times V_S) - (29 \times 5.92) - 14.7 - 3.8 = 406.05 \quad \textbf{(S3)}$$

where the values for V_C, V_H, V_O, V_{Cl}, V_N, V_S are 20.58, 7.24, 14.71, 22.45, 45.60, and 24.43. respectively, $Å^3$. Therefore, the V_{vdW} value of THI is calculated to be 406.05 $Å^3$/molecule. According to $V_{vdW} = 4\pi R_{vdW}^3/3$, we can get the value of van der Waals radius (R_{vdW}) of about 0.46 nm.

In a same manner, the V_{vdW} values of IMI and CLO were calculated to be 0.44 and 0.43 nm, respectively.

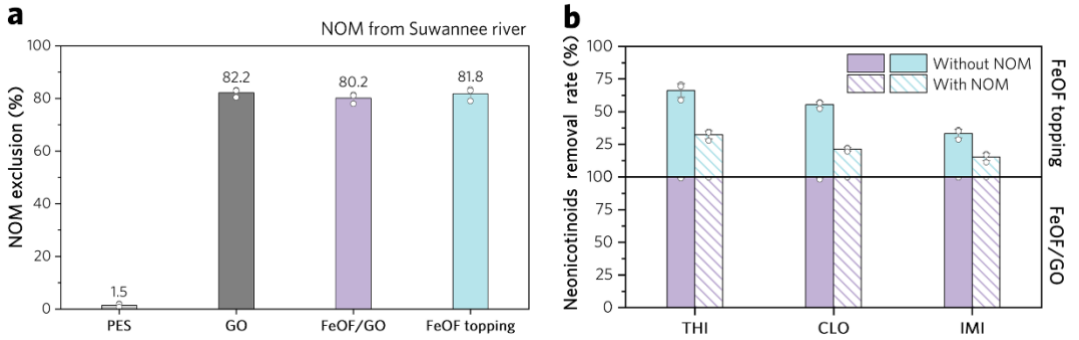

Supplementary Figure 40. **a**, NOM exclusion by membranes ([Suwannee river NOM] = 5 mg L^{-1}). **b**, Neonicotinoids degradation with or without NOM, compositions of contaminated well water were adapted from the recipes of NEWT Center (Nanotechnology Enabled Water Treatment Center, [H_2O_2] = 10 mM, [THI] = [CLO] = [IMI] = 1 μM, pH = 6.2±0.1, [CO_3^{2-}] = 10 mg L^{-1}, [HCO_3^-] = 10 mg L^{-1}, [Cl^-] = 2 mg L^{-1}, [SO_4^{2-}] = 5 mg L^{-1}, [Na^+] = 40 mg L^{-1}, [NOM] = 5 mg L^{-1}, reaction time = 1 h, standard deviations (n = 3) were presented).

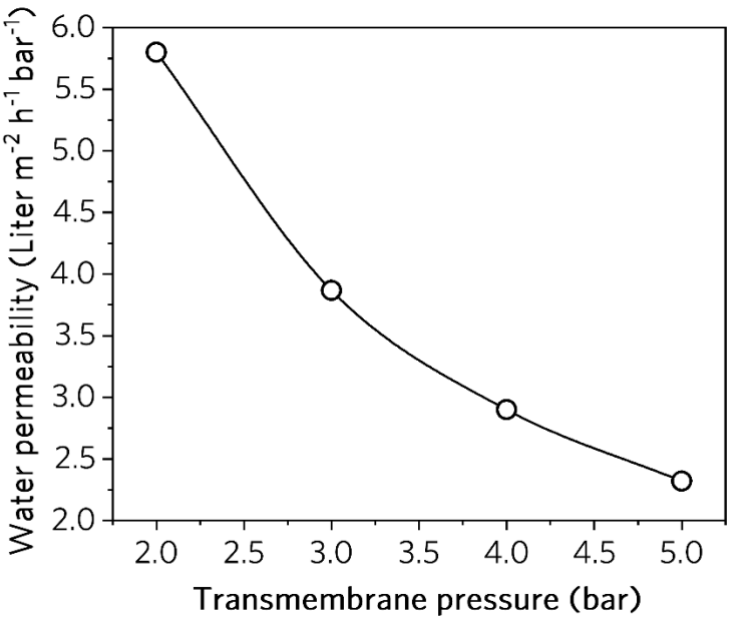

Supplementary Figure 41. Water permeability of FeOF/GO membrane with NOM fouling.

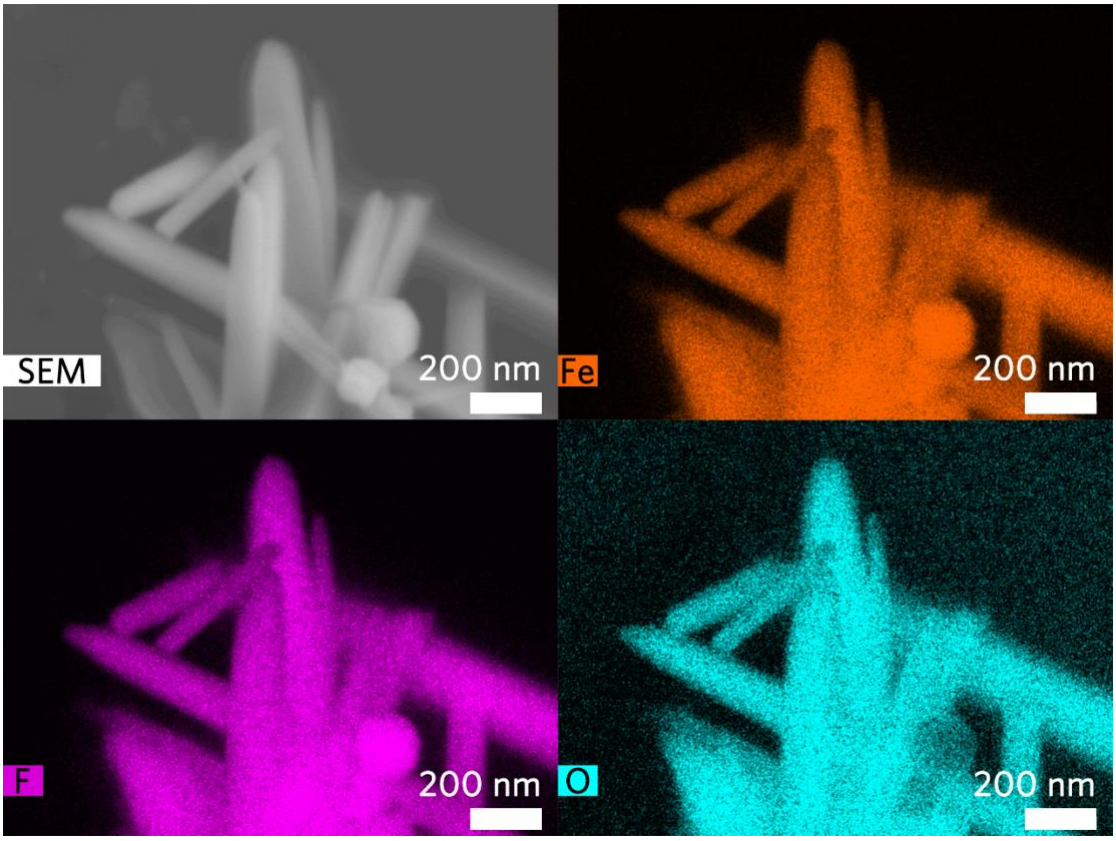

Supplementary Figure 42. SEM and SEM-mapping images of rod-like FeOF.

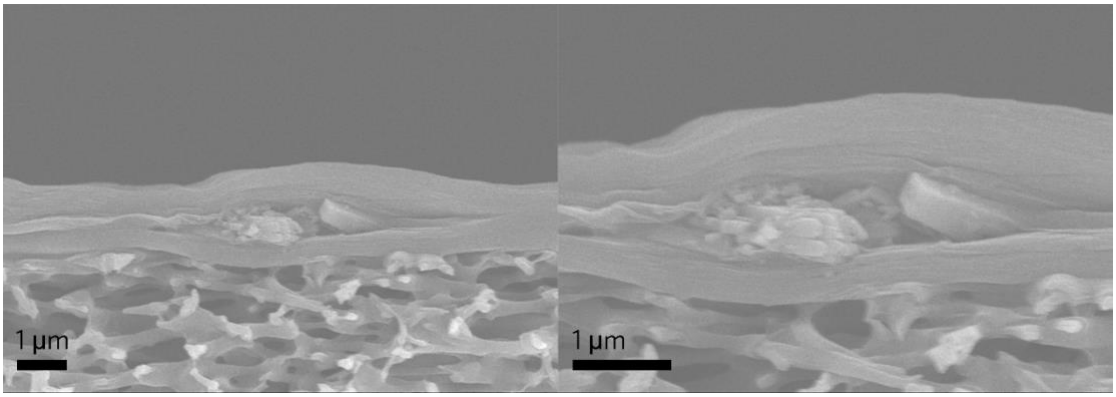

Supplementary Figure 43. Graphene oxide membrane embedded with rod-like FeOF.

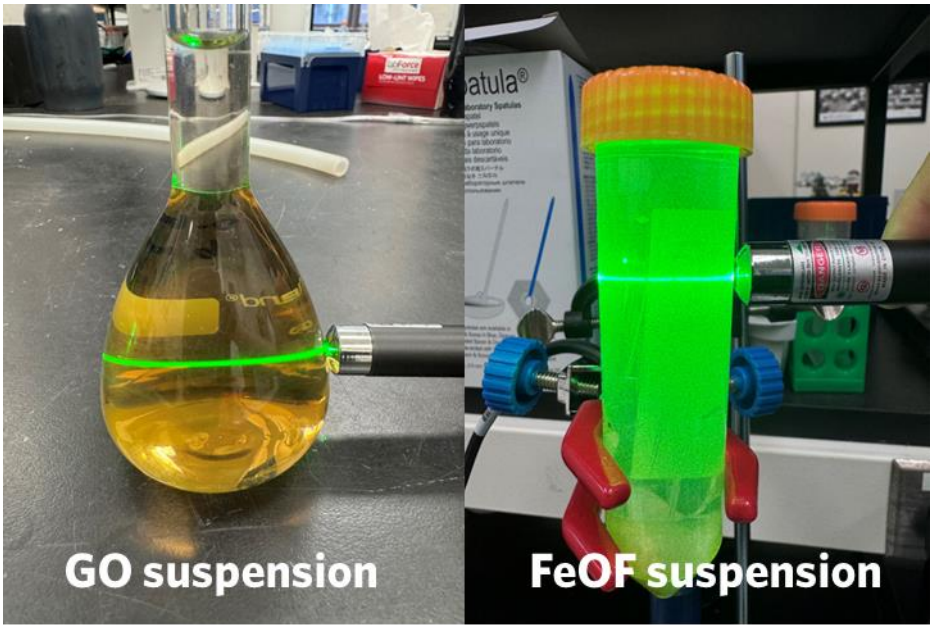

Supplementary Figure 44. GO and FeOF suspensions displaying Tyndall effect under laser emission.

Reference

1. Yu, D. et al. Electronic structure modulation of iron sites with fluorine coordination enables ultra-effective H2O2 activation. Nature Communications 15, 2241 (2024).
2. Sun, M. et al. Reinventing Fenton Chemistry: Iron Oxychloride Nanosheet for pH-Insensitive H2O2 Activation. Environmental Science & Technology Letters 5, 186-191 (2018).
3. Yin, Y., Lv, R., Li, X., Lv, L. & Zhang, W. Exploring the mechanism of ZrO2 structure features on H2O2 activation in Zr–Fe bimetallic catalyst. Applied Catalysis B: Environmental 299, 120685 (2021).
4. Huang, Q.-Q., Liu, H.-Z., Huang, M., Wang, J. & Yu, H.-Q. Ligand-assisted heterogeneous catalytic H2O2 activation for pollutant degradation: The trade-off between coordination site passivation and adjacent site activation. Applied Catalysis B: Environmental 330, 122592 (2023).
5. Sun, H., Xie, G., He, D. & Zhang, L. Ascorbic acid promoted magnetite Fenton degradation of alachlor: Mechanistic insights and kinetic modeling. Applied Catalysis B: Environmental 267, 118383 (2020).
6. Ling, C. et al. Atomic-Layered Cu5 Nanoclusters on FeS2 with Dual Catalytic Sites for Efficient and Selective H2O2 Activation. Angewandte Chemie International Edition 61, e202200670 (2022).
7. Zhang, Y. et al. Iron boride boosted Fenton oxidation: Boron species induced sustainable FeIII/FeII redox couple. Journal of Hazardous Materials 443, 130386 (2023).
8. Yu, H. et al. Facile preparation of coprecipitates between iron oxides and dissolved organic matter for efficient Fenton-like degradation of norfloxacin. Journal of Hazardous Materials 444, 130394 (2023).
9. Ren, Y., Yu, J., Zhang, J., Lv, L. & Zhang, W. An in-situ strategy to analyze multi-effect catalysis in iron-copper bimetals catalyzed Fenton-like processes. Applied Catalysis B: Environmental 299, 120697 (2021).

10. Sun, F. et al. A quantitative analysis of hydroxyl radical generation as H2O2 encounters siderite: Kinetics and effect of parameters. Applied Geochemistry 126, 104893 (2021).
11. Ren, Y. et al. Enhancing the Fenton-like Catalytic Activity of nFe2O3 by MIL-53(Cu) Support: A Mechanistic Investigation. Environmental Science & Technology 54, 5258-5267 (2020).
12. Wang, Y., Zhao, H., Li, M., Fan, J. & Zhao, G. Magnetic ordered mesoporous copper ferrite as a heterogeneous Fenton catalyst for the degradation of imidacloprid. Applied Catalysis B: Environmental 147, 534-545 (2014).
13. Zhang, T. et al. Overcoming Acidic H2O2/Fe(II/III) Redox-Induced Low H2O2 Utilization Efficiency by Carbon Quantum Dots Fenton-like Catalysis. Environmental Science & Technology 56, 2617-2625 (2022).
14. Ding, R.-R. et al. Oxygen vacancy on hollow sphere CuFe2O4 as an efficient Fenton-like catalysis for organic pollutant degradation over a wide pH range. Applied Catalysis B: Environmental 291, 120069 (2021).
15. Zhang, T. et al. Homogeneous Carbon Dot-Anchored Fe(III) Catalysts with Self-Regulated Proton Transfer for Recyclable Fenton Chemistry. JACS Au 3, 516-525 (2023).
16. Yang, Z., Qian, J., Yu, A. & Pan, B. Singlet oxygen mediated iron-based Fenton-like catalysis under nanoconfinement. Proceedings of the National Academy of Sciences 116, 6659-6664 (2019).
17. Xu, P. et al. A Nanoconfined FeCo2O4-Embedded Ceramic Membrane Regulates Electron Transfer in Peroxymonosulfate Activation to Selectively Generate Singlet Oxygen for Water Decontamination. Environmental Science & Technology 58, 17464-17474 (2024).
18. Meng, C. et al. Angstrom-confined catalytic water purification within Co-TiOx laminar membrane nanochannels. Nature Communications 13, 4010 (2022).
19. Wu, X. et al. Single-Atom Cobalt Incorporated in a 2D Graphene Oxide Membrane for Catalytic Pollutant Degradation. Environmental Science & Technology 56, 1341-1351 (2022).